Drag coefficient estimation using flume experiments in shallow non-uniform water flow within emergent vegetation during rainfall

Wei-Jie Wang[a], Wen-Xin Huai[a,*], Sally Thompson[b], Wen-Qi Peng[c,d], Gabriel G. Katul[e,f]

[a] State Key Laboratory of Water Resources and Hydropower Engineering Science, Wuhan University, Wuhan, Hubei 430072, China
[b] Department of Civil and Environmental Engineering, University of California at Berkeley, Berkeley, CA 94720, USA
[c] Department of Water Environment, China Institute of Water Resources and Hydropower Research, Beijing 100038, China
[d] State Key Laboratory of Simulation and Regulation of Water Cycle in River Basin, China Institute of Water Resources and Hydropower Research, Beijing 100038, China
[e] Nicholas School of the Environment, Duke University, Durham, NC 27708, USA
[f] Department of Civil and Environmental Engineering, Duke University, Durham, NC 27708, USA

ARTICLE INFO

ABSTRACT

Vegetation persistence on low-gradient slopes in dryland regions is presumed to be supported by lateral flow of water originating from bare sites with low permeability soil. The hydrodynamics of these flows, which occur during and immediately following intense rainfall events, are challenging to describe with classical approximations to the Saint-Venant equations (SVE). Flume experiments with varying rod density and applied water along the vegetated section are conducted to explore common approximations used to close the SVE when predicting water depth. Guided by these experiments, expressions are then derived that describe the simultaneous effects of spatially uniform vegetation density and rainfall intensity on the drag coefficient (C_d) linking the friction slope to the local kinetic energy head for steady non-uniform flow on a flat surfaces. Spatial variations in C_d through the vegetated patch either exhibit monotonic declines during rain or a non-monotonic 'hump' shape without rain with increasing longitudinal distance into the vegetated section. These spatial variations arise due to the indirect effect of rainfall on the dynamic component of the mean pressure gradient driving flow.

1. Introduction

Water subsidies originating from crusted bare soil and supplied to vegetated sites in arid and semi-arid regions during and immediately after intense rainfall events have well-established ecohydrological significance (Assouline et al., 2015; Bromley et al., 1997; Foti and Ramírez, 2013; Kefi et al., 2008; Klausmeier, 1999; Kletter et al., 2009; Konings et al., 2005; Paschalis et al., 2016; Rietkerk et al., 2002; Thompson et al., 2011, 2008; Valentin and d'Herbès, 1999). These subsidies are particularly significant on low-gradient slopes supporting overland flow, where free water surface gradients instead of ground slopes are responsible for water movement (Rietkerk et al., 2002; Thompson et al., 2011). The hydrodynamics describing these shallow flows constrains the quantity and spatial distribution of water infiltrating into the vegetation root zone. During and immediately after rainfall events, the water level H within the emergent vegetation remains sufficiently shallow that the bulk features of the flow can be reasonably described by the Saint-Venant equation (SVE) (de Saint-Venant, 1871) as described elsewhere (Chen et al., 2013; Thompson et al., 2011).

The application of the SVE to these shallow flows is complicated by multiple factors. Classical simplifications to the SVE such as the kinematic or diffusive wave approximations (French, 1985; Woolhiser and Liggett, 1967), although successfully used to represent overland flow in other contexts, are not applicable here. The kinematic wave approximation fails on low slope gradients, and the diffusive wave approximation cannot be readily applied if advective acceleration (or deceleration) is large. New approximations to the SVE are needed when such non-uniform flows occur within emerging vegetation covering regions with a low slope gradient (Lawrence, 2000). The situation becomes more complicated when such flows are disturbed by rain-action incident on the water surface. The aim here is to advance toward appropriate closure schemes for frictional losses to be used in conjunction with SVE for vegetated surfaces on flat terrain during rainfall events. Controlled experiments on the behavior of non-uniform flow occurring within vegetated canopies and disturbed by extreme rain are a logical starting point for such inquiry. There have been only a limited number of such experiments to date, compared to the wealth of experiments already conducted on uniform-steady flow within submerged or emergent vegetation (Green, 2005; Huai et al., 2009; Huthoff et al., 2007;

James et al., 2004; Järvelä, 2002; Kim et al., 2012; Konings et al., 2012; Kothyari et al., 2009; Liu et al., 2003; Nepf, 2012; Poggi et al., 2004).

When designing such experiments, it is necessary to arrive at some compromises between boundary conditions on the flow and spatial scales that can be resolved by the experiment. During and immediately after an intense storm, the boundary conditions on the SVE must include the rainfall intensity, infiltration rate, vegetation morphology, land surface slope and micro-topography. A complete description of the closure problem to the SVE requires characterizing the effects of large variations across all these factors and their interactions, a task that lies well beyond the scope of a single study or experiment. Consequently, the flume experiments described here address a subset of these factors deemed scientifically uncertain but necessary to the hydrodynamics describing water subsidy. Here, we focus on the interplay between vegetation density and rainfall intensity. Even within this restricted experimental scope, describing all aspects of the hydrodynamics remains a daunting task. Idealized conditions are first considered – steady, non-uniform flow within uniform vegetation, covering a flat slope and subjected to uniform, but intense rainfall. These conditions are selected because they allow the isolation of the direct effect of steady rainfall and its disturbances of the water surface on frictional losses across different vegetation densities. The goal of the laboratory experiments is to provide benchmark data against which conventional models (also analyzed here) and new approximations (proposed here) to frictional losses during extreme rainfall events can be compared when used in conjunction with SVE.

The synthetic vegetation selected here are slender and rigid cylinders broadly resembling the morphology of common perennial desert grasses (e.g., *Hilaria rigida* in California, *Stipagrostis sabulicola* in Namibia, and *Triodia* and *Plectrachne* genuses in Australia). The infiltration contrasts between crusted bare soil patches and permeable vegetated sites, along with the processes of crust formation that can be significantly affected by rainfall, is not explicitly considered. Accommodating a wide range of infiltration contrasts and accounting for rainfall-crust formation interaction is too difficult to experimentally control. Rather than treating these features explicitly, the experiment accommodates their effects by maintaining the type of non-uniformity describing the free water surface shape resulting from the infiltration contrast between crusted soil and vegetation (Rietkerk et al., 2002). A drop-structure is positioned immediately after the vegetated section to ensure that the free water surface directed from the upstream section toward the drop is classified as gradually varied on mild slopes or 'M-type' (French, 1985) as anticipated in such problems (Rietkerk et al., 2002). Such a configuration ensures that the spatially variable free water surface gradient is the main driver for water flow at all locations within the emergent vegetated section. The experiments here feature wide ranging vegetation density (sparse to dense) and *extremal* rainfall intensities, set to unfold the spatial patterns in the drag coefficient (C_d) linking the frictional slope to the kinetic energy head in the SVE during rainfall. The rainfall intensity adopted in the experiment is purposely set to be extreme (4000–8000 mm h^{-1}) – approximately an order of magnitude greater than the highest recorded hourly rainfall rates in the U.S. (Kilauea Plantation, Kauai, Hawaii, January 24, 1956 of approximately 300 mm h^{-1}). While unrealistic in a field setting, we deliberately adopted these extreme rates for the flume experiments for pragmatic reasons – (i) to enable a sufficiently deep water level and ensuing depth non-uniformity that can be accurately resolved through water surface profile imaging while maintaining a sufficiently shallow flow suitable to an SVE approximation. This minimum depth (and its spatial variation) requirement precludes the study of sheet-flow, which may occur in several instances when lateral water is initially created or at some later time as water levels are receding following the passage of the storm. For reference, typical water levels associated with such overland flow can be on the order of 1 cm (Thompson et al., 2011). (ii) Any adjustments to C_d originating from surface water disturbances by rainfall are likely to be amplified in the extreme cases chosen here. The

flume experiments are not intended to exactly replicate a particular hydrological situation or ecosystem configuration but they do provide data on the interplay between mechanisms described by the SVE that are likely to be responsible for causing spatial variability in C_d.

After exploring failures of conventional approaches to modeling water level H using the SVE for the flume experiments here, an operational model linking C_d to vegetated patch properties, rainfall intensity, and water level is proposed. The model mainly summarizes the outcome of the flumes experiments by revealing the key mechanisms responsible for the spatial patterns in $C_d(x)$ in the presence or absence of rain within the confines of the SVE. When spatially averaging these outcomes along the vegetated patch length, the resulting bulk C_d values can also be compared to published data for steady-uniform flow within emergent vegetation.

2. Theory

The flow configuration considered here addresses steady flow within a rectangular flume section of width B and bed slope $S_0 \approx 0$ covered with a cylindrical rod canopy. The rods have diameter D and height h_v, are spaced at an average center-to-center distance of ΔS, and extend over a "vegetated reach" defined by a length L_{veg}. At all spatial locations and flow conditions, $h_v > H$ is maintained. The canopy density is described in terms of the volume fraction occupied by the vegetation, $\phi_{veg} = \pi D^2/(4\Delta S^2)$ (Nepf, 2012). Due to the presence of rods, the width available for the flow within the vegetated section is narrower than B. The effective flow width B_e is derived as follows: The total bed area per unit length along the streamwise direction is B. In this area, flowing water occupies an area of $B(1 - \phi_{veg})$ resulting in an effective flow width $B_e = B(1 - \phi_{veg})$. Similarly, the effective surface area on which rainfall can intercept freely flowing water is given by $A_e = B_e L_{veg}$. The volumetric steady flow rate occurring within the vegetated section in the absence of rainfall is designated by Q_0. When spatially uniform rainfall with rate P is applied over the entire vegetated area A_e, the steady flow rate must increase by some increment $Q_r = PB_e L_{veg}$ above Q_0. At a longitudinal distance $x \in [0, L_{veg}]$ with $x = 0$ set at the starting point (inlet) of the flow into the vegetation zone, the steady flow rate Q_x is given by:

$$Q_x = Q_0 + (PB_e)x = Q_0 + \left(\frac{Q_r}{L_{veg}}\right)x. \tag{1}$$

In addition to changing the mass balance over the vegetated section, the presence of rainfall and vegetation alters the drag coefficient C_d and frictional energy losses, the main focus here. In the absence of any infiltration I, the steady state mean continuity equation and SVE can be expressed as (Thompson et al., 2011; Chen and Liu, 2001)

$$\frac{\partial q_x}{\partial x} = P, \tag{2}$$

$$\frac{\partial}{\partial x}\left(\frac{q_x^2}{H} + \frac{gH^2}{2}\right) + gH(S_f - S_0) = 0, \tag{3}$$

where $q_x = U H$, and U is the area-averaged velocity, g is gravitational acceleration, S_f is the friction slope. Upon combining Eqs. (2) and (3), P can be made to appear explicitly in the conservation of momentum (or SVE) resulting in

$$U\frac{\partial U}{\partial x} + g\frac{\partial H}{\partial x} = g(S_0 - S_f) - \frac{PU}{H}, \tag{4}$$

where the term ($P U/H$) arises from finite steady rain when connecting the mean continuity to the momentum balances. If I is treated as a constant in space set to the infiltration capacity, then P can be readily replaced by $P' = P - I$ without any additional modifications due to finite infiltration. The presence of vegetation introduces an additional drag C_d beyond any side and bed-slope friction (both are negligible

here) that results in an S_f given as (Wang et al., 2015)

$$S_f = \left[\frac{C_d D}{(1 - \phi_{\text{veg}}) \Delta S^2} \right] \frac{U^2}{2g},$$ (5)

where C_d is the (dimensionless) drag coefficient of the vegetation stems to be sought and U is given by

$$U = \frac{Q_x}{B_e H}.$$ (6)

The SVE can be arranged to yield

$$S_f = S_0 - \frac{1}{2} \frac{1}{g} \frac{\partial U^2}{\partial x} - \frac{\partial H}{\partial x} - \frac{PU}{gH},$$ (7)

where $S_f = S_0$ recovers the kinematic wave approximation, and $S_f = S_0 - (\partial H/\partial x)$ recovers the diffusive (or non-inertial) wave approximation. Combining Eqs. (5) and (7), an expression for the dimensionless drag can be derived and is given by

$$C_d = E_{veg} \left(\frac{S_0}{U^2} - \frac{1}{gU} \frac{\partial U}{\partial x} - \frac{1}{U^2} \frac{\partial H}{\partial x} - \frac{P}{gUH} \right),$$ (8)

where $E_{veg} = 2g(1 - \phi_{\text{veg}}) \Delta S^2 / D$ is only impacted by vegetation density and rod diameter (i.e. vegetation properties and its distribution on the surface) and is independent of any flow feature. Here, the choice of variables describing E_{veg} result in units of squared velocity, and this choice of variable is retained because the grouping of these variables arises in many of the equations that follow. A corollary dimensionless quantity may be formed by defining $E_{n,veg} = E_{veg}/(gL_{veg})$. This choice brings another vegetation parameter, L_{veg}, explicitly into the vegetation attributes impacting the flow. The choice of L_{veg} is also a convenient normalizing variable for gradient quantities along x. Both, $E_{n,veg}$ (dimensionless) and E_{veg} (dimensional) are used depending on the case under consideration.

Eq. (8) provides estimates of C_d from a specified rod spacing ΔS and rod diameter D, bed slope S_0, precipitation intensity P, and depth-averaged velocity $U = Q_x/(B_e H)$ that varies with $Q_x(x)$ and $H(x)$. To illustrate how C_d might vary with key dimensionless numbers and why conventional representations fail, Eq. (8) may be formulated as

$$C_d = E_{n,veg} \left(\frac{1}{Fr^2} - \frac{L_{veg}}{U} \frac{\partial U}{\partial x} - \frac{1}{Fr^2} \frac{1}{S_0} \frac{\partial H}{\partial x} - \frac{P}{H} \frac{L_{veg}}{U} \right),$$ (9)

where

$$E_{n,veg} = 2(1 - \phi_{\text{veg}}) \frac{(\Delta S)^2}{DL_{veg}},$$ (10)

and $Fr = U/\sqrt{(S_0 L_{veg})g}$ is a Froude number formed from the bulk velocity U, g and a geometric height $S_0 L_{veg}$, P/H may be interpreted as a hydrological recharge time scale, L_{veg}/U as an advection time scale, $\partial U/\partial x$ is a mean flow distortion time scale induced by the mean vorticity, and $(1/S_0)(\partial H/\partial x)$ may be interpreted as a normalized hydrostatic pressure gradient. In steady-uniform flow with no rain, the SVE equation reduces to a relation between C_d and Fr impacted by the vegetation attributes ϕ_{veg}, ΔS, D, and L_{veg}. Because C_d, by its definition, relates the total kinematic stress (τ_o/ρ, ρ is water density) acting on the flow to U^2 ($\tau_o/\rho = C_d U^2$), and the bulk Reynolds number ($Re_b = H U/\nu$, ν is the kinematic viscosity) dictates how much the viscous stress contributes to τ_o, the SVE may be reduced to a relation between Re_b and Fr. Naturally, all these conventional dimensionless representations of the SVE fail when $S_0 = 0$ and the remaining dimensionless terms in Eq. (9) dominate C_d (instead of Fr), which is one of the motivating factors for the study undertaken here.

To assess the simultaneous effects of intense rain and vegetation density on C_d, two aspects of the C_d variations are presented and discussed. The first considers the longitudinally averaged drag $<C_d> = \int_0^1 C_d(x^+) dx^+$ ($x^+ = x/L_{veg} \leq 1$) across different vegetation densities and rainfall intensities so as to quantify bulk magnitudes and allow comparisons with published studies on uniform vegetated flow in the absence of rainfall (Tanino and Nepf, 2008; Cheng and Nguyen, 2010; Cheng, 2012). The second explores the spatial patterns in the non-uniformity of $C_d(x^+)/ < C_d >$ and unfolds the associated mechanisms responsible for the emergence of these longitudinal patterns across experiments with intense rain and no-rain conditions.

3. Experiments

Flume experiments were conducted at the State Key Laboratory of Water Resources and Hydro-power Engineering Science at Wuhan University (China) to infer $C_d(x)$. The flume is 10 m long with $B = 0.3$ m and $L_{veg} = 0.77$ m. The side walls permit optical access so that the water surface can be imaged. The flume bed was set flat ($S_0 = 0$) and the flow rate was selected to ensure emergent vegetation prevailed ($H/h_v < 1$) across all runs. The steady flow rate was set to $Q_0 = 1.75$ l/s in the absence of rainfall. This Q_0 was needed to guarantee a minimum $H(x)$ for accurate imaging of the water surface as previously discussed.

Vegetation arrangement: Vegetation was represented by an array of plastic cylinders ($D = 8$ mm and $h_v = 250$ mm). The cylinders were positioned on a 10-mm thick plastic board with uniformly spaced holes to accommodate the cylinders and facilitate variation in ϕ_{veg} as shown in Fig. 1. Uniformity in cylinder spacing (i.e. square configuration) was chosen so as to allow an unambiguous definition of ΔS. Other configurations can be chosen (e.g. square versus diamond arrangements) and their effect on C_d has been discussed in a separate study (Wang et al., 2015) but in the absence of rainfall. For dense canopies, such rod configuration differences was shown to have minor effects on C_d when compared to the large variations in ϕ_{veg} considered here.

Four vegetation densities labeled Runs A to D were undertaken with $\phi_{\text{veg}} = 0.269, 0.179, 0.096$ and 0.064, respectively and described in Table 1. Two boards with $\phi_{board} = 0.358$ and 0.128 were used to construct $\phi_{\text{veg}} = 0.269, 0.179, 0.096$, and 0.064. The ϕ_{board} is defined as the fractional area covered by holes on the bare board, i.e., $\phi_{board} = m_0 \pi D^2/4$, with m_0 being the number of holes on the bare board per unit board area. For Runs A, B, C and D, the arrangement is shown in Fig. 1 (b). The presence of a drop structure immediately after the vegetated patch ensures that $H(x)$ crosses critical depth $H_c = (q_L^2/g)^{1/3}$ in the vicinity of the drop where $q_L = (Q_r + Q_0)/B$. The combination of flow rates and L_{veg} also ensured that $H_c < H(x) < h_v$ for all ϕ_{veg}. When the flow attained steady-state, the $H(x)$ for each ϕ_{veg} was determined from images taken by a side view camera delineating the upper surface of the plastic board and the flow surface. The x denotes the downstream distance with $x = 0$ set at the starting point (inlet) of the flow into the vegetation zone. When presenting the raw water level measurements, the normalized $H^+(x) = H(x)/H_0$ where $H_0 = H(0)$ is to be used so as to illustrate the degree of non-uniformity encountered across runs as the water traverses the vegetation patch. The measured flow depths of inlet H_0 and outlet H_L (when $x = L_{veg}$) are presented in Table 1. The measured H_0 here (5–10 cm) is much larger than what is commonly encountered (< 3 cm) in studies of sheet flow on sloping terrain. However, the water surface profile here remained sufficiently gentle so that the pressure gradient can still be approximated from gradients in the water surface profile (i.e. hydrostatic pressure approximation) as required for the usage of SVE in shallow flow.

Rainfall setup: Rainfall was generated by positioning a large container covered at its bottom with filtering nets at $H_{total} = 0.518$ m above the upper surface of the plastic board in the vegetated section. Perforations in the rainfall reservoir had a diameter $D_{rain} = 6$ mm. The reservoir was positioned to provide uniform water application over A_e. Different rainfall intensities were obtained by adjusting the external water supply to the container and densities of filtering nets. For all cases, the effective diameter of raindrops were assumed to be commensurate with D_{rain}. The water supply to the container was held steady
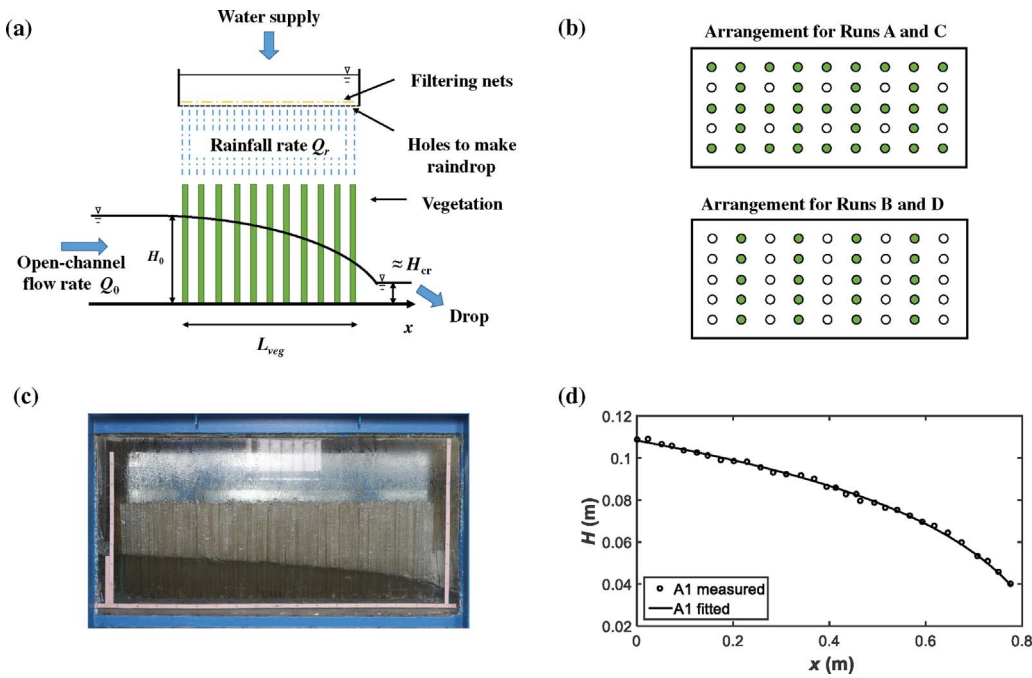
(a)

(b)

(c)

(d)

Fig. 1. (a) Sketch of the rainfall setup in steady nonuniform vegetated flow. (b) Plane view of vegetation arrangement for Runs A to D, where solid circles indicate vegetation and empty circles indicate holes on the board. (c) Images of Run A1 (ϕ_{veg} = 0.269) with rainfall intensity class 1. (d) Comparison between measured and fitted flow depth H in the streamwise direction x used to determine parameters c_1, c_2, and c_3.

and when the water level in the container attained a steady value, the applied rainfall was determined from the supply flow rate. A schematic of the rainfall setup is provided in Fig. 1. Four rainfall intensities were conducted for each of the four ϕ_{veg}. The experiment resulted in sixteen runs, each with different vegetation density and rainfall intensity. Each experimental run is labeled by a capital letter 'A–D', and a number '0–3', where capital letter 'A–D' indicates vegetation density ϕ_{veg} ranging from 0.269 to 0.064 and number '0–3' denotes different rainfall intensities as outlined in Table 1. As earlier noted, P here is at least one order of magnitude larger than extreme rainfall intensities encountered in practice because the focus is on the potential modifications on C_d by large rainfall. However, the more relevant parameter to the flume experiments is not the rainfall intensity per se but the maximum flow rate it generates (= Q_r) with respect to Q_0. This point is made clear by Eq. (9). For the experiments here, Q_r/Q_0 varied from 0 (no rain) to only a modest 20% for the most intense rainfall case. That is, despite the extreme rainfall intensity introduced here, Q_r is only a small contributor to the overall flow rate in the flume experiments. Using the $H(x)$ measurements, all 16 cases were confirmed to be sub-critical and admitted an 'M2-type' water surface shape. To assess whether rainfall additions appear as a continuous stream of water or as fine (mist-like)

water droplets, the Weber number $We = \rho D_{rain} V^2/\sigma$ measuring raindrop inertia to its surface tension (Yarin, 2006) was computed. Here, σ is the water surface tension at room temperature and V is the rain drop velocity as it intercepts the free water surface. The V was not measured but was estimated by assuming potential energies of water droplets at the reservoir location were fully converted to kinetic energy prior to intercepting the free water surface. Air frictional losses across the length over which rain drops were accelerating as they fell and the kinetic energy of water droplets exiting the water reservoir (damped by filtering nets) are ignored. Hence, $V = \sqrt{2gH_{rain}}$, and $H_{rain} = H_{total} - H(x)$. For the configuration here, $We \geq 600$ suggesting rainfall additions above Q_0 resemble those of fine droplets (or mist) and not as continuous water stream held together by surface tension. The large We mimics actual rainfall patterns in field conditions.

4. Results and discussion

4.1. Surface profile model calculations using conventional approaches

Before presenting and discussing the spatial patterns of $C_d(x)$ in nonuniform vegetated flow, an analysis was undertaken to assess how

Table 1
Parameters describing the boundary conditions and flow variables during or with no rain in all experiments.

Run	ϕ_{veg}	H_0 (m)	H_L (m)	Q_r (l/s)	P (mm h^{-1})	$Re_{d,min}$	$Re_{d,max}$	$< Re_d >$
A0	0.269	0.106	0.037	0	0	613	1618	844
A1	0.269	0.109	0.040	0.251	5351	593	1705	869
A2	0.269	0.113	0.042	0.314	6694	571	1701	853
A3	0.269	0.115	0.042	0.386	8229	558	1696	847
B0	0.179	0.101	0.037	0	0	557	1408	755
B1	0.179	0.106	0.038	0.251	4765	531	1541	780
B2	0.179	0.109	0.042	0.314	5960	521	1538	779
B3	0.179	0.113	0.041	0.386	7327	505	1563	772
C0	0.096	0.057	0.025	0	0	905	1960	1181
C1	0.096	0.062	0.026	0.251	4327	854	2111	1206
C2	0.096	0.062	0.027	0.314	5413	798	2055	1158
C3	0.096	0.068	0.029	0.386	6654	766	2052	1137
D0	0.064	0.055	0.028	0	0	889	1742	1128
D1	0.064	0.058	0.029	0.251	4179	843	1914	1161
D2	0.064	0.062	0.032	0.314	5228	809	1804	1120
D3	0.064	0.064	0.032	0.386	6427	778	1785	1100

well conventional approaches predict $H(x)$ reported in the flume experiments here. The raw images acquired by the side-camera and used in the analysis here are featured in the appendix. The conventional approaches considered include Manning's empirical formula relating S_f to a constant roughness coefficient n, and literature values for C_d derived for uniform flow within a rigid rod canopy. The formulations for C_d evaluated here include those for isolated cylinders and for cases where 'blocking' occurs (Wang et al., 2015). Their outcome is a C_d that is not constant along x but varies with a local Reynolds number. Because the Froude number $Fr_b = U/\sqrt{gH} < 1$ for all cases here, the calculations of water surface profile were conducted from the outlet where $H(L) \approx H_c$ to the inlet opposite to the flow direction.

4.1.1. Manning's formula

Assuming locally uniform flow, Manning's empirical formula can be used to relate S_f to H using

$$S_f = \left(\frac{nU}{R_h^{2/3}} \right)^2, \tag{11}$$

where n is Manning's roughness coefficient assumed constant along x, U is the depth-averaged velocity, and $R_h \approx H$ is the hydraulic radius. This approximation is equivalent to replacing the vegetation drag by surface stresses acting along R_h. Substituting Eq. (11) into the momentum balance in Eq. (4) allows for the calculation of $H(x)$ when specifying n. Fig. 2 compares measured and modeled $H(x)$ for no-rain cases (Runs A0, B0, C0 and D0) and extreme rain cases (Runs A3, B3, C3 and D3) when setting $n = 0.01, 0.1, 0.5$ and 1 independent of x for illustration. It is evident that the imaged water surface profile cannot be reasonably reproduced for all cases no matter what the value of n is with or without rainfall. The value $n = 0.5$ appears to reasonably describe a subset of the cases (A0, A3, B0 and B3).

4.1.2. C_d for uniform flow from literature

The previous analysis was repeated but retaining the effects of

vegetation using drag coefficients reported for isolated cylinders (hereafter referred to as $C_{d\text{-}iso}$) and eliminating wall friction. The $C_{d\text{-}iso}$ is not constant and can be described based on a local Reynolds number ($Re_d = \rho D\, U/\mu$) using (Cheng, 2012)

$$C_{d\text{-}iso} = 11\,Re_d^{-0.75} + 0.9\Gamma_1(Re_d) + 1.2\Gamma_2(Re_d), \tag{12}$$

where

$$\Gamma_1(Re_d) = 1 - \exp\left(-\frac{1000}{Re_d} \right), \tag{13}$$

and

$$\Gamma_2(Re_d) = 1 - \exp\left[-\left(\frac{Re_d}{4500} \right)^{0.7} \right]. \tag{14}$$

Because wakes produced by the rod canopy can introduce either sheltering or blockage effects, the drag coefficient $C_{d\text{-}array}$ deviates from its isolated counterpart as reported from numerous studies on uniform flow (Ishikawa et al., 2000; James et al., 2004; Tanino and Nepf, 2008; Liu et al., 2003; Ferreira et al., 2009; Kothyari et al., 2009; Stoesser et al., 2010). The outcome of these experiments (again mainly for uniform flow) may be summarized by

$$C_{d\text{-}array} = 50(Re_v)^{-0.43} + 0.7\left[1 - \exp\left(-\frac{Re_v}{15000} \right) \right], \tag{15}$$

where the vegetation-related Reynolds is $Re_v = UR_v/\nu$, and vegetation-related hydraulic radius R_v is

$$R_v = \frac{\pi}{4} \frac{1 - \phi_{\text{veg}}}{\phi_{\text{veg}}} D. \tag{16}$$

The R_v includes the simultaneous effects of D and ϕ_{veg}. The above $C_{d\text{-}iso}$ and $C_{d\text{-}array}$ were used to solve $H(x)$ in the SVE. The results are featured in Fig. 3. From this figure, it can be surmised that adopting literature expressions for $C_{d\text{-}iso}$ or $C_{d\text{-}array}$ derived for uniform flow, while an improvement over the constant n, under-predict $H(x)$ with or without
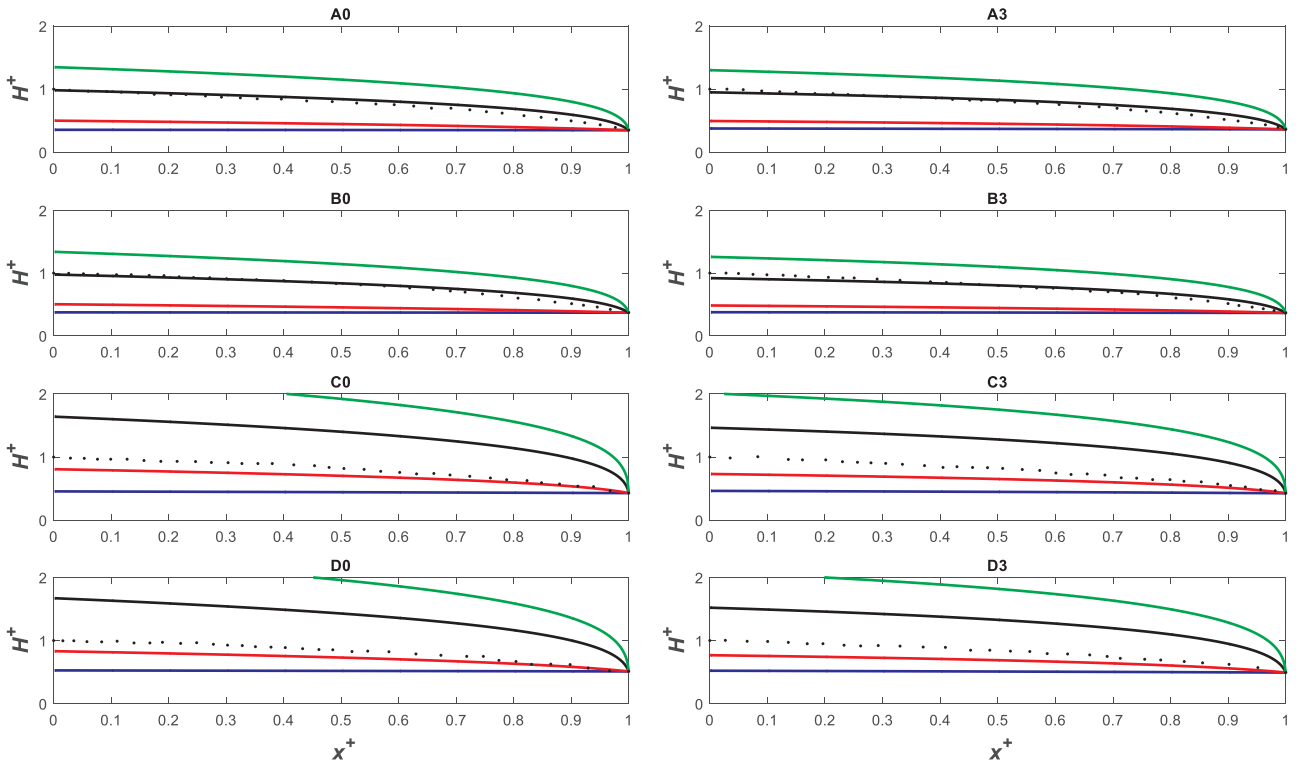

Fig. 2. Comparison between measured and modeled $H^+(x^+)$ using four n values, where dots are measured $H^+(x^+)$ and blue lines are modeled $H^+(x^+)$ using $n = 0.01$, red lines are modeled $H^+(x^+)$ using $n = 0.1$, black lines are modeled $H^+(x^+)$ using $n = 0.5$, and green lines are modeled $H^+(x^+)$ using $n = 1$. (For interpretation of the references to color in this figure legend, the reader is referred to the web version of this article.)
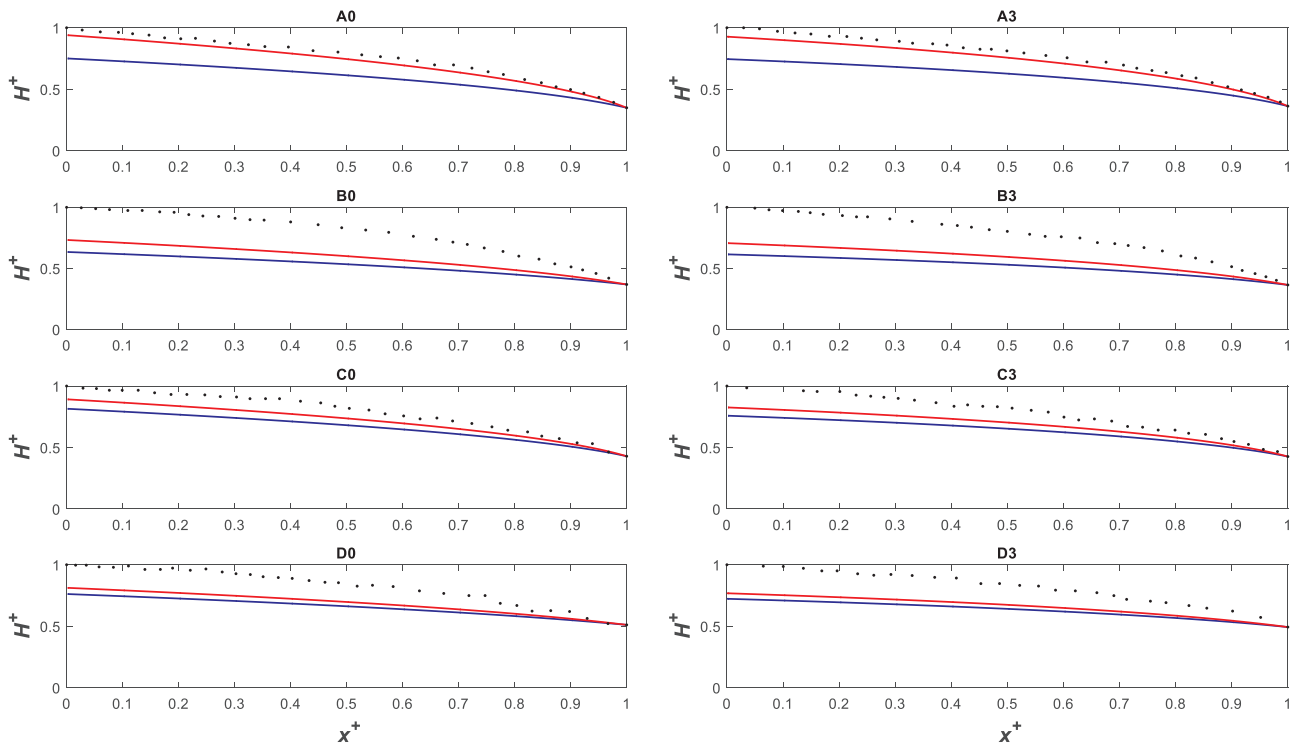
Fig. 3. Comparison between measured and modeled H^+ ($= H/H_0$) along with x^+ ($= x/L_{veg}$) using $C_{d\text{-}iso}$ and $C_{d\text{-}array}$ derived for uniform flow, where dots are measured $H^+(x^+)$, blue lines are modeled $H^+(x^+)$ when using $C_{d\text{-}iso}$, and red lines are modeled $H^+(x^+)$ when using $C_{d\text{-}array}$.

rainfall. It is precisely these failures that motivated the inquiry into the spatial patterns of $C_d(x)$ using the flume experiments here above and beyond what can be predicted from local Re_d or Re_v.

4.2. Post-processing of the water surface images and determining $< C_d >$ in nonuniform vegetated flow

Because Eq. (8) requires estimating longitudinal gradients in H and U that are prone to measurement errors (especially during rain), post processing of the inferred $H(x)$ from images is undertaken prior to computing $\partial H/\partial x$ and $\partial U/\partial x$. For an 'M2-type' water level surface (the case here), a logarithmic function reasonably describes $H(x)$ variations (Wang et al., 2015) and is adopted here. Prior to estimating C_d from Eq. (8), the imaged $H(x)$ is first fitted to $H = c_1 \ln|x - c_2| + c_3$. The $\partial H/\partial x = c_1/(x - c_2)$ at any x is then computed using c_1 and c_2, where parameters c_1, c_2 and c_3 are obtained from nonlinear regression between imaged $H(x)$ and distance x as illustrated in Fig. 1(c) and (d). The fitting parameters c_1, c_2 and c_3 are determined for each run and are shown in Table 2. These coefficients offer a data summary of the shape of measured $H(x)$. Comparison between measured and fitted flow depth in streamwise direction for all cases is illustrated in Fig. 4.

Fig. 5(a) shows the resulting M2 shape of the dimensionless level $H'^+ = (H(x) - H_c)/(H_0 - H_c)$ against x^+. Interestingly, this normalization for water level (i.e. H'^+ instead of $H^+ = H(x)/H_0$) reasonably collapses fitted $H(x)$ with and without rainfall. Because L_{veg} and B are constants, this data collapse implies water level differences for a given x^+ across runs can be attributed to differences in H_0 and H_c.

The fitted $H(x)$ for each run is now used to infer $C_d(x)$ and subsequently, $< C_d >$. To compare these estimates with experiments conducted for steady-uniform flow within vegetation in the absence of rain (Tanino and Nepf, 2008; Cheng and Nguyen, 2010; Cheng, 2012), $< C_d >$ is presented as a function of the longitudinally averaged element Reynolds number $< Re_d > = D < U > /\nu$ in Fig. 5(b), where $< U >$ is longitudinally averaged flow velocity. Minimum, maximum and longitudinally averaged Reynolds number $Re_{d,min}$, $Re_{d,max}$ and $< Re_d >$ calculated based on fitted $H(x)$ for each case were

Table 2
Regression parameters describing the imaged water surface profile for all the cases. These parameters offer a summary of all the water surface profile measurements.

Run	ϕ_{veg}	c_1	c_2	c_3
A0	0.269	3.839E−02	9.341E−01	1.071E−01
A1	0.269	3.847E−02	9.327E−01	1.109E−01
A2	0.269	3.992E−02	9.306E−01	1.153E−01
A3	0.269	4.013E−02	9.274E−01	1.181E−01
B0	0.179	3.573E−02	9.250E−01	1.052E−01
B1	0.179	3.797E−02	9.286E−01	1.103E−01
B2	0.179	4.003E−02	9.424E−01	1.121E−01
B3	0.179	4.038E−02	9.319E−01	1.160E−01
C0	0.096	1.954E−02	9.595E−01	5.801E−02
C1	0.096	2.136E−02	9.725E−01	6.129E−02
C2	0.096	2.471E−02	1.001E+00	6.500E−02
C3	0.096	2.577E−02	1.000E+00	6.771E−02
D0	0.064	1.825E−02	9.790E−01	5.658E−02
D1	0.064	2.019E−02	9.904E−01	5.956E−02
D2	0.064	2.104E−02	1.013E+00	6.156E−02
D3	0.064	2.285E−02	1.036E+00	6.363E−02

shown in Table 1. The goal of this comparison is to experimentally illustrate modifications to C_d due to rain and flow non-uniformity. Fig. 5(b) shows that the computed $< C_d > /E_{n,veg}$ exhibited an expected decline with increasing $< Re_d >$. Run-to-run $< C_d >$ variations are explained by $< Re_d >$, once differences in vegetation densities are accounted for through $E_{n,veg}$. The $< C_d > /E_{n,veg}$ approximately declined as $< Re_d > ^{-\alpha}$ with increasing $< Re_d >$, where $\alpha \approx 4$ ($\alpha = 1$ is for Laminar flow around isolated cylinders). Using linear regression, $\ln(< C_d > /E_{n,veg}) = -4.14\ln(< Re_d >) + 31.80$ was computed with a coefficient of determination (R^2) = 0.98. Increasing α beyond unity implies that $< C_d > /E_{n,veg}$ approaches a constant value at lower $< Re_d >$ threshold. The $< C_d > /E_{n,veg}$ variation with $< Re_d >$, assuming non-interacting cylinders is also computed and shown in Fig. 5(b). For all $< Re_d >$, the estimated $< C_d >$ exceeds its isolated cylinder counterpart for the same Re_d as expected from Section 4.1.2. At large $< Re_d >$, deviations between these $< C_d > /E_{n,veg}$ estimates become
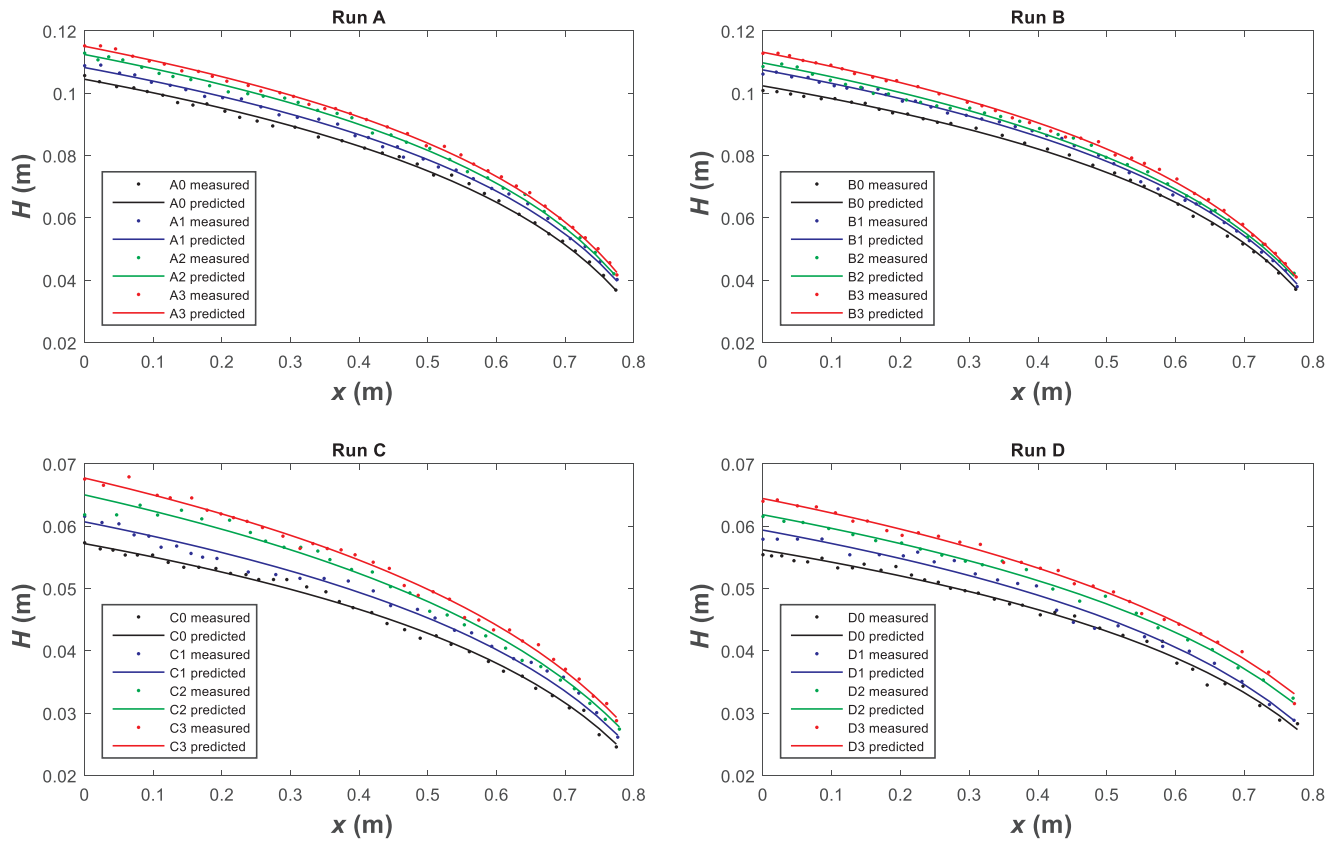
Fig. 4. Comparison between measured and fitted flow depth in streamwise direction for all cases. The dots indicate measurements and different lines are the fitted logarithmic functions.

smaller. Likewise, comparing the $<C_d>/E_{n,veg}$ with the case where wake interferences are allowed but referenced to $<Re_d>$, suggests that the drag coefficient here remains larger consistent with expectations from the analysis in Section 4.1.2. Because $<C_d>/E_{n,veg}$ appears to follow the same $<Re_d>^{-\alpha}$ curve for rain and no-rain cases, flow non-uniformity (rather than rain splash effects) may explain some

differences between the drag estimates here and published estimates for uniform flow.

4.3. Spatial patterns of $C_d(x)$ in nonuniform vegetated flow

The spatial patterns of $C_d(x)$ inferred from SVE using measured $H(x)$
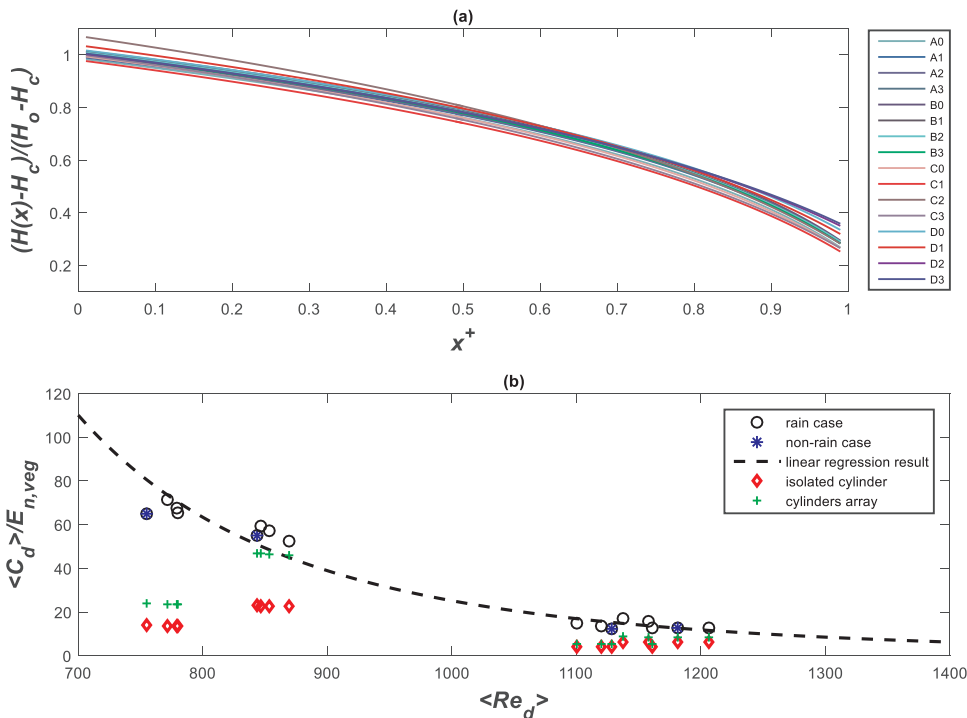
Fig. 5. (a) Variation of normalized water level $H'^+(x)$ versus normalized distance $x^+ = x/L_{veg}$ illustrating near similarity across all runs. (b) Variations of $<C_d>/E_{n,veg}$ with $<Re_d>$ across all experiments (filled circles are for no rain and open circles are with rain). The curve $\ln(<C_d>/E_{n,veg}) = -4.14 \ln(<Re_d>) + 31.80$ is shown as dashed line (coefficient of determination, $R^2 = 0.98$). The diamonds are $C_d/E_{n,veg}$ based on isolated cylinders and the pluses are for interacting wakes within cylinders.
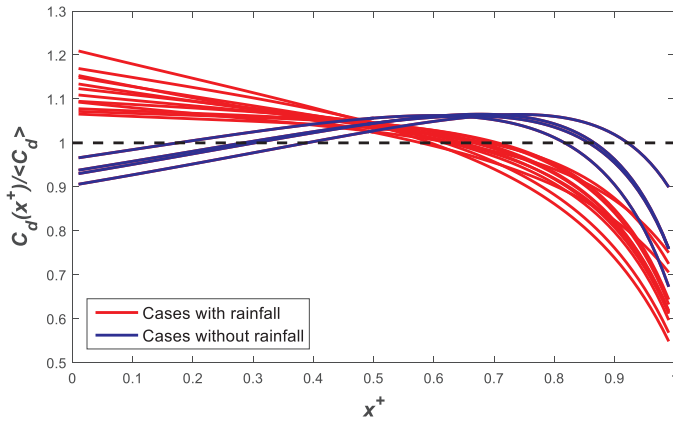
Fig. 6. Variations of $C_d(x^+)/ < C_d >$ with x^+ showing two types of spatial patterns when rain is on (red lines) and off (blue lines). (For interpretation of the references to color in this figure legend, the reader is referred to the web version of this article.)

are presented using the experiments here. The effects of $H(x)$ non-uniformity on the spatial patterns in $C_d(x)$ are shown by plotting $C_d(x)/ < C_d >$ against x^+ in Fig. 6. This normalization references the non-uniformity in C_d across all runs to previously studied values of $< C_d >$. One of the novel and unexpected findings here is the emergence of two divergent spatial patterns that can be distinguished based on the presence or absence of rain despite the small Q_r/Q_0. Without rain, $C_d(x)/ < C_d >$ increases and then decreases with increasing x^+ forming a hump-shape that has been studied elsewhere (Wang et al., 2015). In the presence of intense rain, $C_d(x)/ < C_d >$ monotonically decreases with increasing x^+. These patterns remain approximately similar across runs despite large variations in vegetation density and rainfall intensity. To explain the occurrences and differences between spatial patterns, the terms impacting $C_d(x)$ in Eq. (8) were analyzed here at all x.

4.4. Factors influencing C_d

The normalized contributions of all the main terms in the SVE to C_d can be expressed as

$$C_d = (1 - \phi_{\text{veg}}) \frac{\Delta S^2}{DL_{\text{veg}}} (S_0^* + P^* - A^* - R^*), \tag{17}$$

where the bed slope effect term S_0^* is

$$S_0^* = S_0 \left(\frac{L_{\text{veg}}}{U^2/2g} \right). \tag{18}$$

The pressure term P^* is

$$P^* = \left(-\frac{\partial H}{\partial x} \right) \left(\frac{L_{\text{veg}}}{U^2/2g} \right). \tag{19}$$

The advection term A^* is

$$A^* = \left(\frac{\partial U}{\partial x} \right) \left(\frac{2L_{\text{veg}}}{U} \right). \tag{20}$$

The rainfall term R^* is

$$R^* = P \left(\frac{2L_{\text{veg}} B_e}{Q_x} \right). \tag{21}$$

The $S_0 = 0$ in the flume experiments here. Hence, the shape of $C_d - Re_d$ curve is primarily determined by three terms P^*, A^* and R^*. show the interplay between terms P^*, A^* and R^* along with x^+ for Runs A to D. The shape of $P^* - A^*$ is almost the same as $P^* - A^* - R^*$. The shape of P^* for all 16 cases is shown in Fig. 11. For the no-rainfall case, P^* exhibits a non-monotonic increase along x^+. Conversely, P^* shows a decreasing trend along x^+ for cases with rainfall (Runs A1 to A3, B1 to B3, C1 to C3 and D1 to D3) in Fig. 11.

From Fig. 11, it can be argued that the shape of C_d is primarily determined by P^*, in which $-\partial H/\partial x$ is increasing and $1/U^2$ is decreasing with x^+. The product of an increasing and decreasing functions yields different trend outcomes with increasing x^+. Specifically, product of $-\partial H/\partial x$ and $1/U^2$, which forms P^*, exhibits a non-monotonic shape for the no-rainfall case (Runs A0, B0, C0 and D0), while it shows decreasing trends with x^+ for rainfall cases (Runs A1 to A3, B1 to B3, C1 to C3 and D1 to D3). The pressure gradient contribution emerged as most dominant in all 16 cases and at all x. A comparison in Fig. 12 between C_d computed using all the terms in Eq. (8) and computed using only the pressure gradient contribution (hereafter referred to as $C_{d,p}$) for all measured $H(x)$ makes this point clear. Any spatial non-uniformity in $C_d(x)$ can be evaluated with respect to its $C_{d,p}$ component given as.

$$C_{d,p} = (1 - \phi_{\text{veg}}) \frac{\Delta S^2}{DL_{\text{veg}}} \left(-\frac{\partial H}{\partial x} \right) \left(\frac{L_{\text{veg}}}{U^2/2g} \right). \tag{22}$$

This component can be expressed as a function of another Froude number Fr_H using

$$C_{d,p} = 2(1 - \phi_{\text{veg}}) \frac{\Delta S^2}{DL_{\text{veg}}} Fr_H^{-2}, \tag{23}$$

where $Fr_H = U/\sqrt{(S_H L_{\text{veg}})g}$, and $S_H = -\partial H/\partial x$ is the water surface slope. Once again, when expressing $C_{d,p}$ as a function of Re_d, the SVE equation can be reduced to a relation between two dimensionless numbers: Fr_H and Re_d, where ϕ_{veg}, ΔS, D and L_{veg} impact its shape. Because S_H is explicitly known in $H(x)$ and after some algebra, $C_{d,p}$ can be made as a function of E_{veg}, B, $H(x)$, x as well as Q_r and Q_0 (all employed by the SVE) using

$$C_{d,p} \approx E_{\text{veg}} \left(\frac{B_e}{Q_0} \right)^2 c_1 \exp \left(\frac{H_0 - H(x)}{c_1} \right) \frac{H(x)^2}{[1 + (Q_r/Q_0)(x/L_{\text{veg}})]^2}. \tag{24}$$

Eq. (24) shows a relation between $C_d(x)$ and a product of two terms that vary with $H(x)$. The first term is an exponential arising from $-\partial H/\partial x$ that monotonically increases with increasing x due to the 'M2' shaped $H(x)$ forced by the downstream boundary condition (drop structure). The second is a quadratic term arising from U^{-2} that decreases as $H(x)^2$ due to continuity considerations in the absence of rain ($Q_r = 0$). As noted earlier, the product of a gradually increasing and decreasing function with x explains the 'hump shape'. Specifically, when $Q_r = 0$, Eq. (24) must exhibit a maximum determined from $dC_{d,p}/dH = 0$ occurring for $H = 2c_1$ when $x = c_2 - \exp(2 - c_3/c_1)$.

When $Q_r > 0$, the decreasing $H(x)^2$ term decreases even more rapidly with increasing x due to contributions from $[(Q_r/Q_0)(x/L_{veg})]^{-2}$ (i.e. the U^{-2} shape dominates the spatial pattern of $C_{d,p}(x)$). This additional reduction due to finite Q_r partly counters the exponential increases at small x thereby resulting in a monotonically declining $C_{d,p}$ with x. When $Q_r > 0$, it can be mathematically shown from Eq. (24) that $dC_{d,p}/dx \neq 0$ at any $0 < x^+ < 1$ when

$$\frac{Q_r}{Q_0} > \frac{L_{\text{veg}}(H(x) - 2c_1)}{2c_2 c_3 + x(2c_1 - 3c_3) + (2c_2 - 3x)(H(x) - c_3)}. \tag{25}$$

The maximum value of the right hand-side of above equation was 0.13 for the experiments here (i.e. preset L_{veg}, c_1, c_2, and c_3), which means $Q_r/Q_0 > 0.13$ is sufficient to dampen the hump-shape in $C_d(x)$ observed for the no-rain cases where $Q_r = 0$. For all the 3 intense rainfall cases, Q_r/Q_0 ranges from 0.14 to 0.22, meaning $Q_r/Q_0 > 0.13$ is satisfied. Hence, the formulation in Eq. (24) explains the two distinct spatial patterns in $C_d(x)$ inferred from measured $H(x)$, indicating that $C_d(x)$ shows the 'hump shape' when $Q_r/Q_0 \leq 0.13$ and appears monotone decreasing feature when $Q_r/Q_0 > 0.13$. This is the sought result.

5. Conclusion

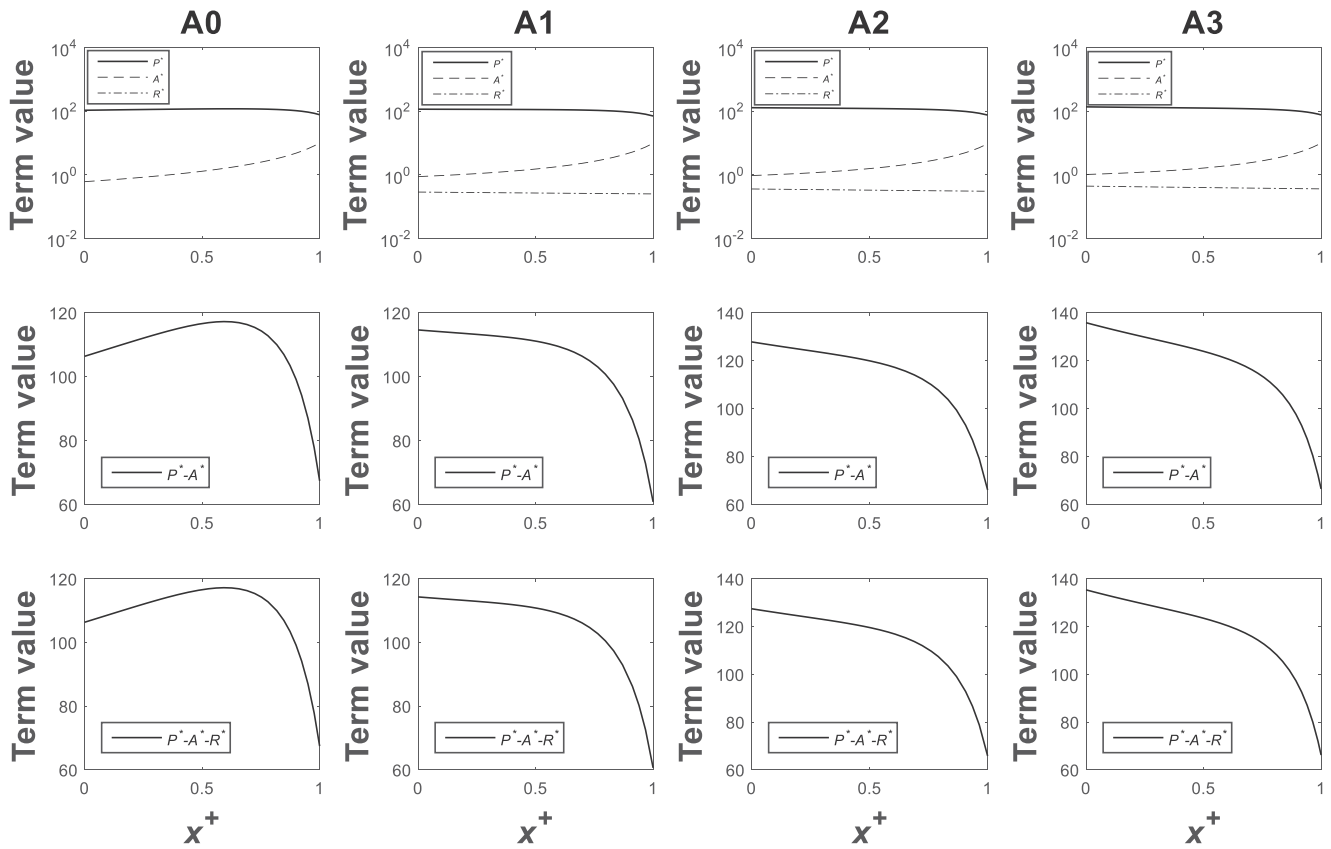The volume and distribution of water flowing from crusted bare soil

Fig. 7. Analysis the shape of C_d along normalized streamwise direction x^+ for Run A ($\phi_{veg} = 0.269$), and every column denotes the case with different rainfall intensity.
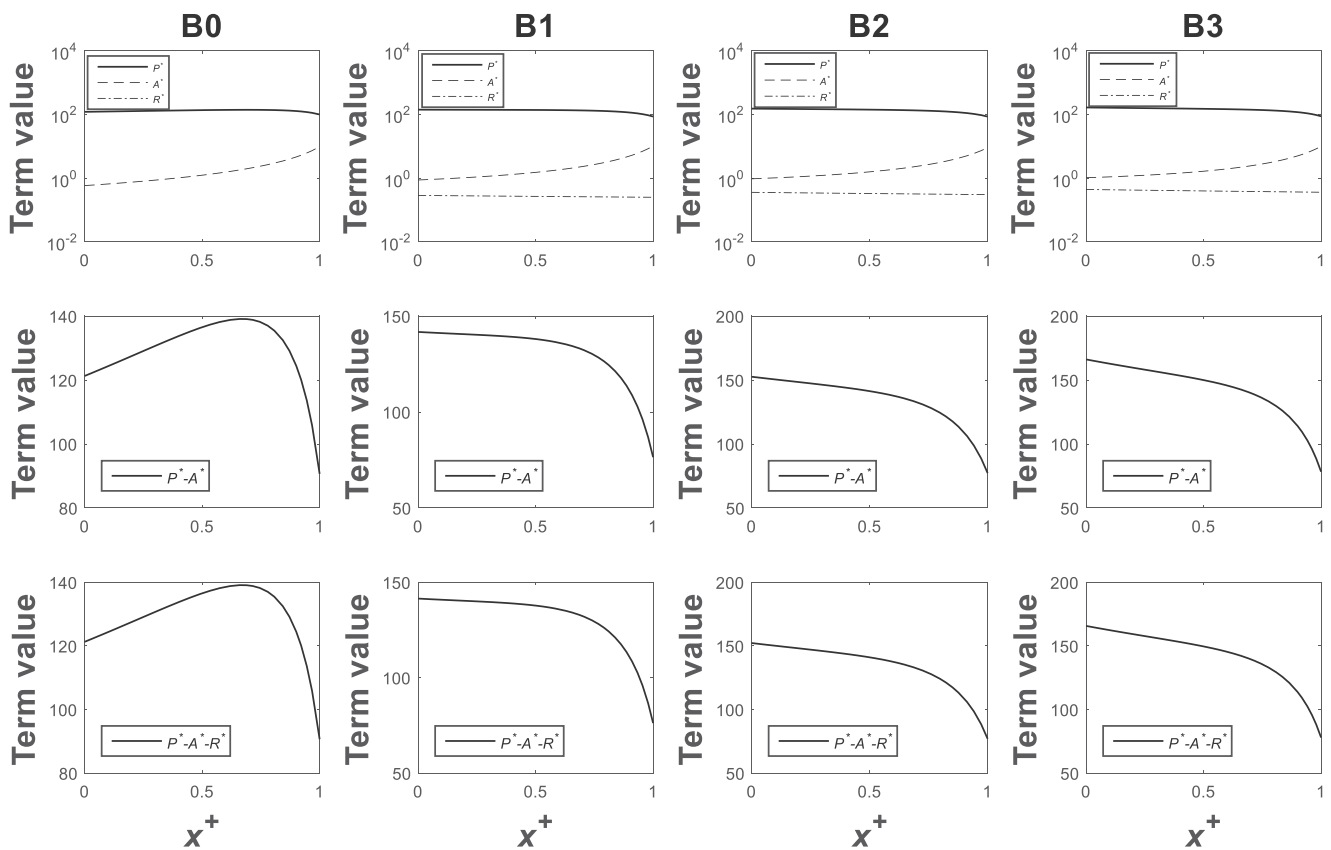

Fig. 8. Analysis the shape of C_d along normalized streamwise direction x^+ for Run B ($\phi_{veg} = 0.179$), and every column denotes the case with different rainfall intensity.
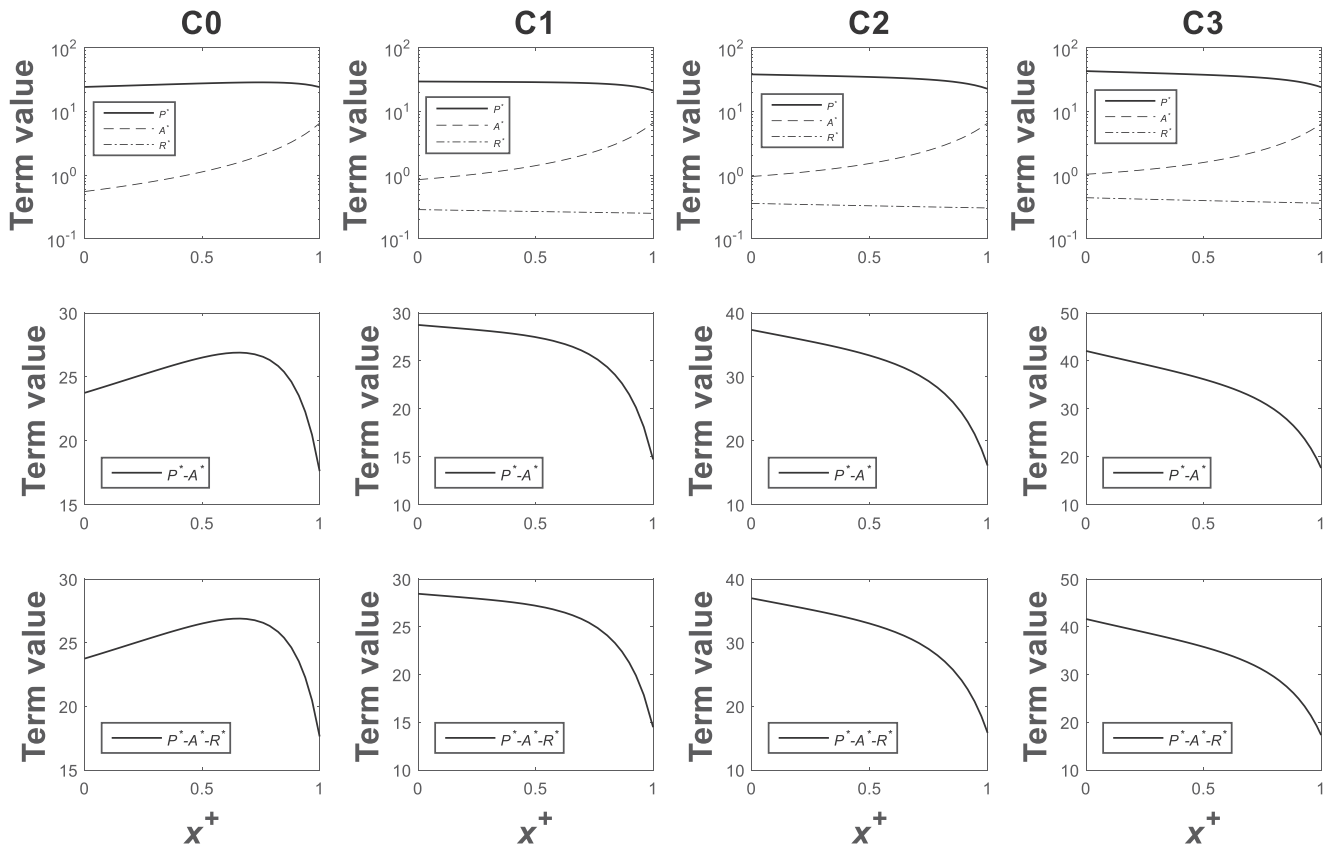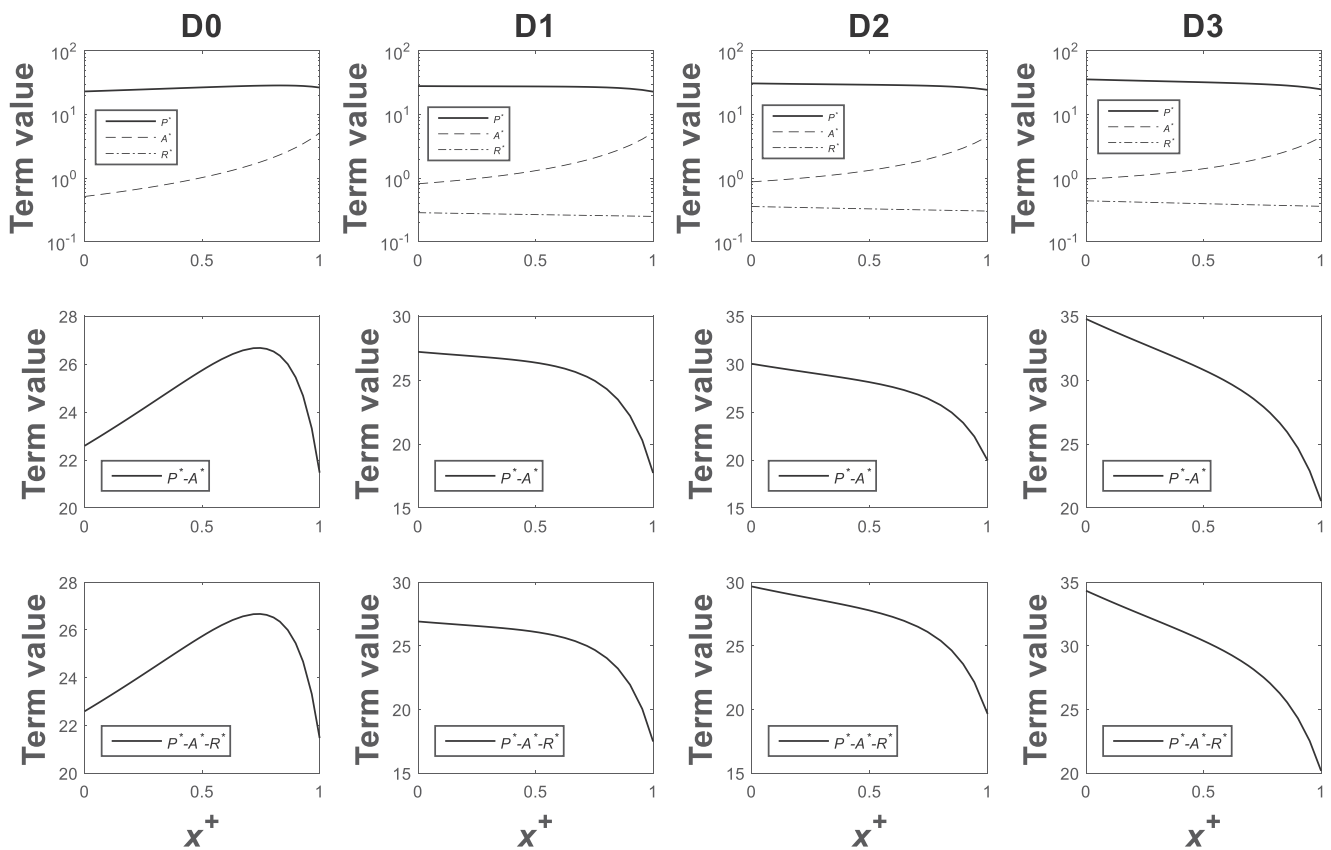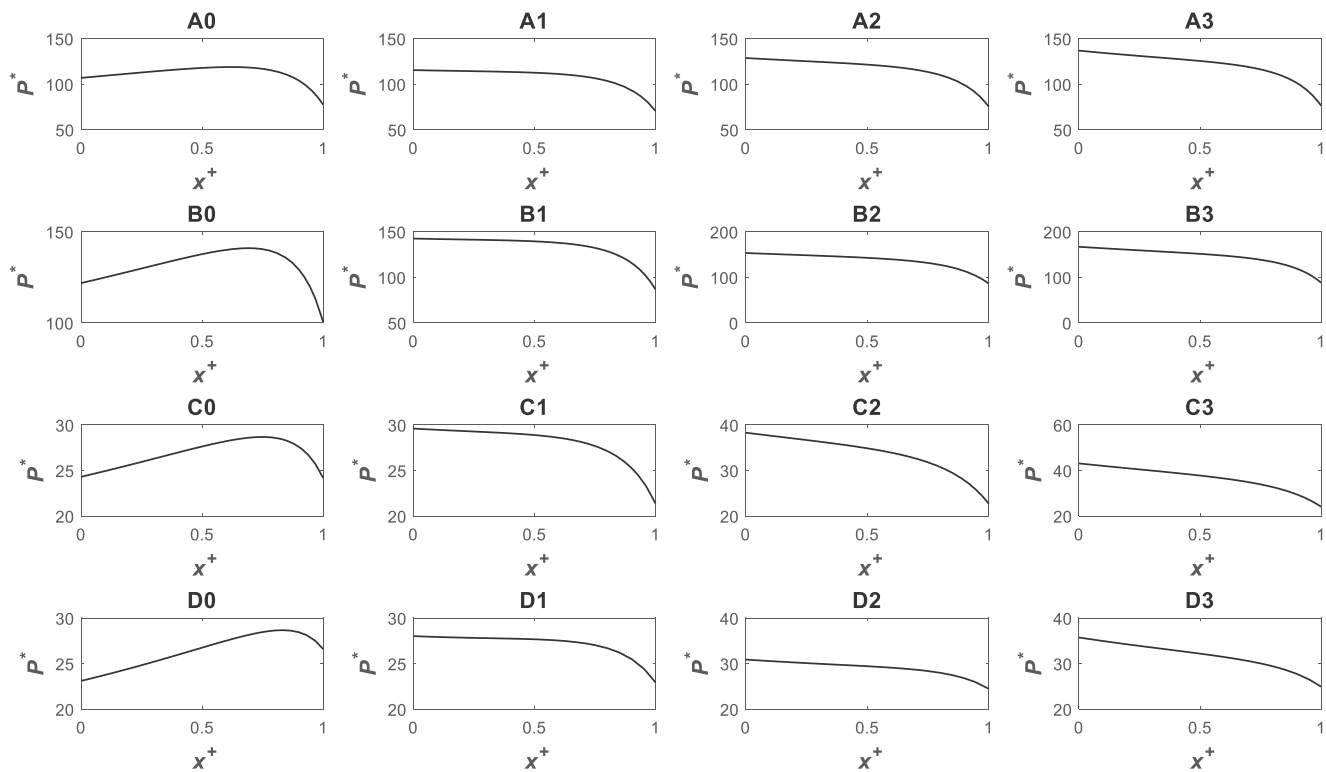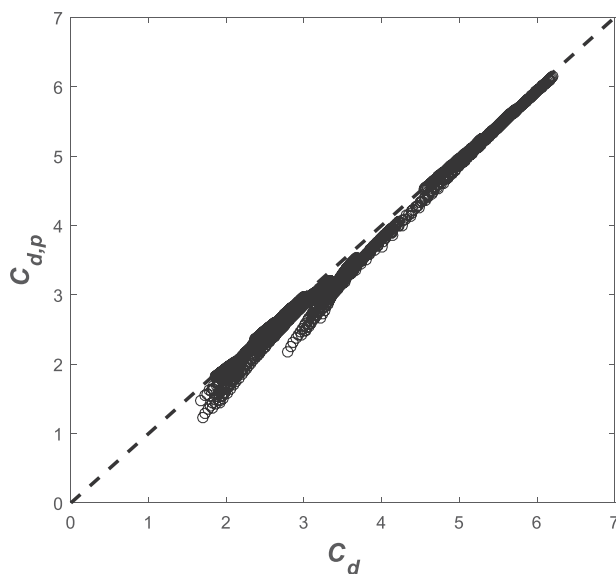
Fig. 9. Analysis the shape of C_d along normalized streamwise direction x^+ for Run C (ϕ_{veg} = 0.096), and every column denotes the case with different rainfall intensity.

Fig. 10. Analysis the shape of C_d along normalized streamwise direction x^+ for Run D (ϕ_{veg} = 0.064), and every column denotes the case with different rainfall intensity.

Fig. 11. Analysis the shape of P^* along normalized streamwise direction x^+ for all the cases.

Fig. 12. Comparison between computed $C_d(x)$ using all the terms and $C_{d,p}(x)$ using only the pressure gradient contribution. The one-to-one line is shown for reference.

inhomogeneity in boundary conditions such as the drop structure used in the flume experiments here or variable infiltration rates in field conditions. One of the barriers to accounting for such flow non-uniformity on S_f or the associated drag coefficient is the lack of benchmark experiments, especially during rainfall events. Using flume experiments and detailed analysis on the various terms impacting C_d, we are beginning to address some aspects of this knowledge gap. The measured water surface profiles here were designed to maintain their 'M2' shape for both rain and no-rain cases. Besides vegetation attributes (E_{veg}), all factors (see Eq. (17)) such as bed slope effect term, pressure term, advection term and rainfall term were considered to make quantitative impact analysis on C_d. Comparison in Fig. 12 shows that the main term impacting C_d in all cases was the pressure gradient, which can be expressed as a function of Reynolds number Re_d. The direct bed-slope effect on C_d was removed by virtue of the setup (flat-ground). The flow rate associated with rainfall additions impacted C_d indirectly through alterations in the spatial variation of the depth-averaged velocity. Spatial variations in C_d exhibited either a monotonic decline (during extreme rain) or a 'hump' shape (no rain) with increasing x. With proper normalization, it was shown that these two spatial patterns maintained similar shapes across wide ranging canopy densities and extreme rainfall application rates. A simplified model to be used with SVE accounting for $C_d(x)$ variations with vegetation density and diameter, patch length, H, Q_0, Q_r (during rain), and x was proposed building on the near self-similar shapes of H'^+ across runs. The broader impact of this work is to bridge advances in non-uniform canopy flows with ecohydrological studies of the functioning of patchy dryland ecosystems, where lateral fluxes targeted here appear critical for ecological function. It should be noticed that the experiments conducted here were based on steady flow and emergent vegetation with constant diameter. Reynolds number Re_d for all cases is under 2000. Extreme rainfall intensity P is set varying roughly from 4000 to 8000. Specifically, the formulation for C_d proposed here adds realism to any hydrodynamic accounting of the feedback mechanism by which bare soil areas elevate plant available water above and beyond those determined by intense rainfall incident over vegetation.

to vegetated sites on flat ground during and following rainfall has been conventionally modeled using (i) the SVE closed by a Manning-type equation (e.g. Chen et al., 2013) with a constant Manning coefficient associated with the vegetated section or (ii) a proportionality (or diffusion-like) constant multiplying $\partial H/\partial x$ (Kefi et al., 2008; Klausmeier, 1999; Kletter et al., 2009; Konings et al., 2005). These two formulations cannot fully recover all aspects of the spatial variations in S_f driving the flow, meaning that alternative approaches are required.

Rainfall effects on S_f have rarely been considered in this context despite their likely ubiquity. Flow non-uniformity arises in such situations even for steady flow within uniform emergent vegetation subjected to a uniform rainfall. This non-uniformity is mainly produced by

Acknowledgments

References

Assouline, S., Thompson, S., Chen, L., Svoray, T., Sela, S., Katul, G., 2015. The dual role of soil crusts in desertification. J. Geophys. Res. Biogeosci. 120 (10), 2108–2119. http://dx.doi.org/10.1002/2015JG003185.

Bromley, J., Brouwer, J., Barker, A., Gaze, S., Valentine, C., 1997. The role of surface water redistribution in an area of patterned vegetation in a semi-arid environment, south-west Niger. J. Hydrol. 198 (1–4), 1–29. http://dx.doi.org/10.1016/S0022-1694(96)03322-7.

Chen, L., Liu, Q., 2001. On the equation of overland flow and one dimensional equations for open channel flow with lateral inflow. Mech. Eng. 4, 21–23 (in Chinese).

Chen, L., Sela, S., Svoray, T., Assouline, S., 2013. The role of soil-surface sealing, microtopography, and vegetation patches in rainfall-runoff processes in semiarid areas. Water Resour. Res. 49 (9), 5585–5599. http://dx.doi.org/10.1002/wrcr.20360.

Cheng, N.-S., Nguyen, H.T., 2010. Hydraulic radius for evaluating resistance induced by simulated emergent vegetation in open-channel flows. H. Hydraul. Eng. 137 (9), 995–1004. http://dx.doi.org/10.1061/(ASCE)HY.1943-7900.0000377.

Cheng, N.-S., 2012. Calculation of drag coefficient for arrays of emergent circular cylinders with pseudofluid model. H. Hydraul. Eng. 139 (6), 602–611. http://dx.doi.org/10.1061/(ASCE)HY.1943-7900.0000722.

de Saint-Venant, A.B., 1871. Theorie du mouvement nonpermanent des eaux, avec application aux crues des rivieres et a l'introduction des mare es dans leurs lits. C. R. Acad. Sci. 73, 237–240.

Ferreira, R.M., Ricardo, A.M., Franca, M.J., 2009. Discussion of "Laboratory investigation of mean drag in a random array of rigid, emergent cylinders" by Yukie Tanino and Heidi M. Nepf. H. Hydraul. Eng. 135 (8), 690–693. http://dx.doi.org/10.1061/(ASCE)HY.1943-7900.0000021.

Foti, R., Ramírez, J.A., 2013. A mechanistic description of the formation and evolution of vegetation patterns. Hydrol. Earth Syst. Sci. 17 (1), 63–84. http://dx.doi.org/10.5194/hess-17-63-2013.

French, R.H., 1985. Open-channel Hydraulics. McGraw-Hill, New York.

Green, J.C., 2005. Modelling flow resistance in vegetated streams: review and development of new theory. Hydrol. Process. 19 (6), 1245–1259. http://dx.doi.org/10.1002/hyp.5564.

Huai, W.-X., Zeng, Y.-H., Xu, Z.-G., Yang, Z.-H., 2009. Three-layer model for vertical velocity distribution in open channel flow with submerged rigid vegetation. Adv. Water Resour. 32 (4), 487–492. http://dx.doi.org/10.1016/j.advwatres.2008.11.014.

Huthoff, F., Augustijn, D., Hulscher, S.J., 2007. Analytical solution of the depth-averaged flow velocity in case of submerged rigid cylindrical vegetation. Water Resour. Res. 43 (6). http://dx.doi.org/10.1029/2006WR005625.

Ishikawa, Y., Mizuhara, K., Ashida, S., 2000. Effect of density of trees on drag exerted on trees in river channels. J. For. Res. 5 (4), 271–279. http://dx.doi.org/10.1007/BF02767121.

Järvelä, J., 2002. Flow resistance of flexible and stiff vegetation: a flume study with natural plants. J. Hydrol. 269 (1), 44–54. http://dx.doi.org/10.1016/S0022-1694(02)00193-2.

James, C., Birkhead, A., Jordanova, A., O'sullivan, J., 2004. Flow resistance of emergent vegetation. J. Hydraul. Res. 42 (4), 390–398. http://dx.doi.org/10.1080/00221686.2004.9728404.

Kefi, S., Rietkerk, M., Katul, G.G., 2008. Vegetation pattern shift as a result of rising atmospheric CO_2 in arid ecosystems. Theor. Popul. Biol. 74 (4), 332–344. http://dx.doi.org/10.1016/j.tpb.2008.09.004.

Kim, J., Ivanov, V.Y., Katopodes, N.D., 2012. Hydraulic resistance to overland flow on surfaces with partially submerged vegetation. Water Resour. Res. 48 (10). http://dx.doi.org/10.1029/2012WR012047.

Klausmeier, C.A., 1999. Regular and irregular patterns in semiarid vegetation. Science 284 (5421), 1826–1828. http://dx.doi.org/10.1126/science.284.5421.1826.

Kletter, A., Von Hardenberg, J., Meron, E., Provenzale, A., 2009. Patterned vegetation and rainfall intermittency. J. Theor. Biol. 256 (4), 574–583. http://dx.doi.org/10.1016/j.jtbi.2008.10.020.

Konings, A.G., Dekker, S.C., Rietkerk, M., Katul, G.G., 2005-2012. Drought sensitivity of patterned vegetation determined by rainfall-land surface feedbacks. J. Geophys. Res. Biogeosci. 116 (G4). http://dx.doi.org/10.1029/2011JG001748.

Konings, A.G., Katul, G.G., Thompson, S.E., 2012. A phenomenological model for the flow resistance over submerged vegetation. Water Resour. Res. 48 (2). http://dx.doi.org/10.1029/2011WR011000.

Kothyari, U.C., Hayashi, K., Hashimoto, H., 2009. Drag coefficient of unsubmerged rigid vegetation stems in open channel flows. J. Hydraul. Res. 47 (6), 691–699. http://dx.doi.org/10.3826/jhr.2009.3283.

Lawrence, D., 2000. Hydraulic resistance in overland flow during partial and marginal surface inundation: experimental observations and modeling. Water Resour. Res. 36 (8), 2381–2393. http://dx.doi.org/10.1029/2000WR900095.

Liu, D., Diplas, P., Fairbanks, J., Hodges, C., 2003–2012. An experimental study of flow through rigid vegetation. J. Geophys. Res. Earth Surf. 113 (F4). http://dx.doi.org/10.1029/2008JF001042.

Nepf, H.M., 2012. Flow and transport in regions with aquatic vegetation. Annu. Rev. Fluid Mech. 44, 123–142. http://dx.doi.org/10.1146/annurev-fluid-120710-101048.

Paschalis, A., Katul, G.G., Fatichi, S., Manoli, G., Molnar, P., 2016. Matching ecohydrological processes and scales of banded vegetation patterns in semi-arid catchments. Water Resour. Res. 1–68. http://dx.doi.org/10.1002/2015WR017679.

Poggi, D., Porporato, A., Ridolfi, L., Albertson, J., Katul, G., 2004. The effect of vegetation density on canopy sub-layer turbulence. Bound. Layer Meteorol. 111 (3), 565–587. http://dx.doi.org/10.1023/B:BOUN.0000016576.05621.73.

Rietkerk, M., Boerlijst, M.C., van Langevelde, F., HilleRisLambers, R., van de Koppel, J., Kumar, L., Prins, H.H., de Roos, A.M., 2002. Self-organization of vegetation in arid ecosystems. Am. Nat. 160 (4), 524–530. http://dx.doi.org/10.1086/342078.

Stoesser, T., Kim, S., Diplas, P., 2010. Turbulent flow through idealized emergent vegetation. H. Hydraul. Eng. 136 (12), 1003–1017. http://dx.doi.org/10.1061/(ASCE)HY.1943-7900.0000153.

Tanino, Y., Nepf, H.M., 2008. Laboratory investigation of mean drag in a random array of rigid, emergent cylinders. H. Hydraul. Eng. 134 (1), 34–41. http://dx.doi.org/10.1061/(ASCE)0733-9429(2008)134:1(34.

Thompson, S., Katul, G., McMahon, S.M., 2008. Role of biomass spread in vegetation pattern formation within arid ecosystems. Water Resour. Res. 44 (10). http://dx.doi.org/10.1029/2008WR006916.

Thompson, S., Katul, G., Konings, A., Ridolfi, L., 2011. Unsteady overland flow on flat surfaces induced by spatial permeability contrasts. Adv. Water Resour. 34 (8), 1049–1058. http://dx.doi.org/10.1016/j.advwatres.2011.05.012.

Valentin, C., d'Herbès, J.-M., 1999. Niger tiger bush as a natural water harvesting system. Catena 37 (1), 231–256. http://dx.doi.org/10.1016/S0341-8162(98)00061-7.

Wang, W.-J., Huai, W.-X., Thompson, S., Katul, G.G., 2015. Steady nonuniform shallow flow within emergent vegetation. Water Resour. Res. 51 (12), 10047–10064. http://dx.doi.org/10.1002/2015WR017658.

Woolhiser, D.A., Liggett, J.A., 1967. Unsteady, one-dimensional flow over a plane: the rising hydrograph. Water Resour. Res. 3 (3), 753–771. http://dx.doi.org/10.1029/WR003i003p00753.

Yarin, A., 2006. Drop impact dynamics: splashing, spreading, receding, bouncing. Annu. Rev. Fluid Mech. 38, 159–192. http://dx.doi.org/10.1146/annurev.fluid.38.050304.092144.